PAPER

Check for updates

Visualizing diverse lithium growth and stripping behaviors in anode-free solid-state batteries with *operando* X-ray tomography

Stephanie Elizabeth Sandoval,†[a,b] Douglas Lars Nelson,[b] Hari Sridhara,[b]
Talia A. Thomas,[a] John A. Lewis,[b] Kelsey Anne Cavallaro,[b] Pavel Shevchenko,[c]
Neil P. Dasgupta, [d,e] Francois L. E. Usseglio-Viretta,[f] Donal P. Finegan [f] and
Matthew T. McDowell *[a,b]

Anode-free solid-state batteries (SSBs), which eliminate the need for lithium metal use during cell assembly, have the potential to enable high energy densities and simplified manufacturing. However, the factors that control lithium growth/stripping at the anode current collector are not well understood. Here, we use *operando* X-ray microcomputed tomography to comprehensively image and quantify lithium deposition and stripping under various conditions in three different Li|Li$_6$PS$_5$Cl|current collector cells, revealing diverse behavior that depends on interface morphology, cell resistance, and solid-state electrolyte (SSE) microstructure. A cell with high resistance exhibits extensive lithium filament growth across the entire current collector interface, with filaments that grow around pre-existing pores in the SSE rather than lithium filling these pores. Lithium filament formation is partially reversible, with the cracks shrinking as lithium metal is stripped. Uniform lithium deposition is achievable at low current densities in low-resistance cells, whereas higher current densities in these cells cause an increase in interfacial roughness, which is correlated with subsequent filamentary growth at the edges of the cell. These results provide insight into filamentary *vs.* planar lithium growth and highlight that the evolution of lithium is sensitively dependent on SSE microstructure and electrochemical processes.

Broader context

Anode-free solid-state batteries could enable high energy density, but short circuiting induced by lithium filament growth can limit performance. Here, *operando* X-ray microcomputed tomography is used to directly investigate and visualize lithium deposition and stripping in anode-free solid-state batteries. The insights gained from these experiments provide new understanding of fundamental interfacial phenomena and could guide the engineering of solid-state battery materials.

Introduction

Solid-state batteries (SSBs) hold promise as an improved energy storage technology, since they potentially offer higher energy densities, improved safety, and enhanced stability compared to lithium-ion batteries.[1–7] Solid-state electrolytes (SSEs) could enable the use of lithium metal anodes; however, lithium anode implementation in SSBs has been hindered by the reactive nature of lithium and its complex evolution during cycling.[8–11] Anode-free battery architectures, in which lithium is deposited *in situ* on a current collector during the first charge, are of particular interest, as they eliminate the need for reactive lithium metal foil use during manufacturing and also enable high energy density.[12–18] However, the

[a]George W. Woodruff School of Mechanical Engineering, Georgia Institute of Technology, Atlanta, GA, 30332, USA. E-mail: mattmcdowell@gatech.edu
[b]School of Materials Science and Engineering, Georgia Institute of Technology, Atlanta, GA, 30332, USA
[c]Advanced Photon Source, Argonne National Laboratory, Lemont, IL 60439, USA
[d]Department of Mechanical Engineering, University of Michigan, Ann Arbor, Michigan 48109, USA
[e]Department of Materials Science and Engineering, University of Michigan, Ann Arbor, Michigan 48109, USA
[f]National Renewable Energy Laboratory, 15013 Denver W. Parkway, Golden, CO, 80401, USA
†Current address: Institute of Inorganic and Analytical Chemistry, University of Münster, 48149 Münster, Germany.

morphological evolution of lithium is even more challenging to control in anode-free SSBs than in lithium-excess SSBs.[19–23] This is because nucleation and growth must occur on a foreign current collector, and the lack of excess lithium inventory beyond that contained in the cathode requires extremely high coulombic efficiency (CE) for long-term cycling.[17]

The mechanisms governing lithium metal behavior in SSBs have been intensively investigated in recent years, resulting in an improved understanding of the differences between SSBs and liquid-electrolyte batteries. Lithium stripping at relatively high rates can lead to void formation at the interface in SSBs, reducing the extent of interfacial contact.[22–25] Void formation has been observed in lithium-excess SSBs as well as anode-free SSBs.[12–14,26] The loss of interfacial contact increases the effective current density at the remaining contact points,[13,23] promoting non-uniform lithium deposition in subsequent charging cycles and eventually leading to lithium filament growth and short circuiting.[19–21]

Filamentary growth of lithium through the SSE is a critical challenge limiting the performance of SSBs. Various mechanisms have been proposed to govern filamentary growth and penetration of lithium, including initiation at surface defects, crack propagation, and effects arising from electronic conductivity.[21,27–30] In general, understanding the details of how lithium evolves during deposition and stripping is necessary to prevent unwanted filamentary growth and is crucial to enable more reliable SSBs.

A variety of advanced characterization techniques, such as *operando* optical microscopy,[30–33] *ex situ* cryogenic/plasma focused-ion beam (FIB) scanning electron microscopy (SEM),[20,33–35] and transmission electron microscopy (TEM)[36–38] have been useful for investigating the behavior of lithium metal in SSBs, often using lithium symmetric cells. Many of these techniques, however, are limited to probing localized interfacial regions. In contrast, *operando* X-ray computed tomography (CT) allows for imaging of material evolution within an entire cell during charge/discharge.[39] Several prior studies have used *operando* X-ray CT to capture the formation of voids and the growth of lithium filaments within SSBs.[22,23,40–44] Two studies recently tracked the evolution of filament-driven cracks in lithium symmetric cells with sulfide SSEs, showing that some cracks initiate and propagate across the electrolyte first, followed by lithium deposition into the tips of these cracks.[42,43] Similarly, *operando* X-ray CT has captured the initiation of filaments *via* spallation cracking at the lithium|SSE interface, with subsequent propagation of a crack *via* wedge-opening.[44] While these studies have been useful for enhancing our understanding of the growth of lithium in SSBs, most studies investigating lithium growth mechanisms have focused on single filamentary growth events or localized regions, and sometimes with impractical associated electrochemistry (such as high voltages in *operando* cells). Since other experiments have suggested that the evolution of lithium can vary depending on the electrochemical conditions,[23,24] the SSE microstructure,[16,29,45] and the nature of engineered interfaces,[46–48] there is a need to further understand lithium

dynamics under various possible growth and stripping scenarios in realistic cell environments.

Here, we use *operando* X-ray microcomputed tomography (µCT) to track and quantify the morphology of lithium metal at the current collector|SSE interface under varied deposition and stripping conditions in anode-free solid-state cells with lithium counter electrodes. By examining cells with different electrochemical conditions and SSE microstructures, this study aims to go beyond prior isolated observations to shed light on the diverse behavior of lithium that is present in SSBs. We visualize lithium evolution across 2 mm-diameter interfaces in three different cells: (A) a cell with high resistance that features extensive filamentary growth across the interface, (B) a cell featuring relatively uniform deposition and stripping, and (C) a cell featuring uniform deposition at lower current densities that transitions to filamentary growth at higher current densities. Quantifying the lithium morphology evolution in these cells provides important insights. Assorted filament morphologies were observed in the first cell, with branching growth of filaments as well as filaments that grew around (rather than within) pre-existing pores in the SSE. Filament-induced cracks containing lithium shrunk upon stripping of lithium under the applied stack pressure, but ~20% of the crack volume remained after one cycle. In cells with lower resistance, a transition from uniform planar growth of lithium to filamentary growth at higher current densities was found to be accompanied by an average roughening of the interfacial morphology, and localized filaments were primarily found near the edges of electrodes at these higher current densities. The quantified evolution of lithium morphology in various SSB cells herein provides new understanding of the factors governing lithium metal anodes in SSBs, and our work highlights the need to consider diverse electro-chemo-mechanical scenarios to understand behavior.

Results and discussion

Operando X-ray µCT imaging was used to examine the growth behavior of lithium in three different cells, denoted cases A, B, and C. These solid-state cells were fabricated using a 10 µm thick Cu foil working electrode modified with a thin Ag or Au layer, a lithium metal counter electrode, and a Li_6PS_5Cl (LPSC) SSE. LPSC powders with two different particle sizes were used: coarse-grained LPSC (typically 10–100 µm particle size; case A) and fine-grained LPSC (typically 1–5 µm particle size; cases B and C). These different LPSC particle sizes are associated with different electrochemical behavior, as detailed subsequently. The cells all featured thin (~100 nm) Ag or Au films deposited onto the current collectors; these films have been shown to enhance the uniformity of lithium deposition and stripping through a mechanism in which the Ag or Au layer alloys and dealloys each cycle, providing for more uniform nucleation and growth of lithium to improve CE and performance.[12,17] These interlayers both promoted reliable behavior of the *oper-*

ando cells, and the differences of the behavior of the Au *vs.* Ag for the purpose of this study are considered negligible, as both alloy materials have previously been shown to support similarly favorable lithium growth behavior despite undergoing slightly different morphological transformations.[12] Cells with a diameter of 2 mm were constructed in custom-built tomography cell casings specifically designed for X-ray µCT imaging (Fig. 1a).[12,13] These cells are able to apply a stack pressure of ~10 MPa while maintaining an airtight seal.

Operando imaging during galvanostatic cycling of the half cells was carried out by collecting tomographic scans every 15 min. In each tomographic scan, the cell was rotated 180° and 1200 projection images were collected at discrete angular intervals, for a total scan time of ~5 min. Three-dimensional (3D) datasets were reconstructed from the tomographic scans with voxel sizes of 1.8 µm, 1.7 µm, and 1.4 µm for cases A, B, and C, respectively. Full experimental details are contained in the SI.

Electrochemical behavior

First, we discuss the electrochemical behavior of all three cells, and in subsequent sections we connect the electrochemistry to microstructural evolution. Fig. 1b shows the galvanostatic electrochemical curves for the three cells during the *operando* experiments. For all three cases, lithium was first deposited on the working electrode using a current density of 0.5 mA cm^{-2} to reach an areal capacity of 3 mAh cm^{-2}. The cell voltages during this deposition process are different for each cell, with case A showing higher overpotential than the other two cases. Shortly after the onset of deposition, each galvanostatic curve exhibits characteristic features consistent with interlayer alloying, in agreement with previous work.[12,17] In case A, the typical alloying plateaus associated with Au are not observed above 0 V; instead, an alloying plateau appears below 0 V, likely due to the higher resistance in this cell.
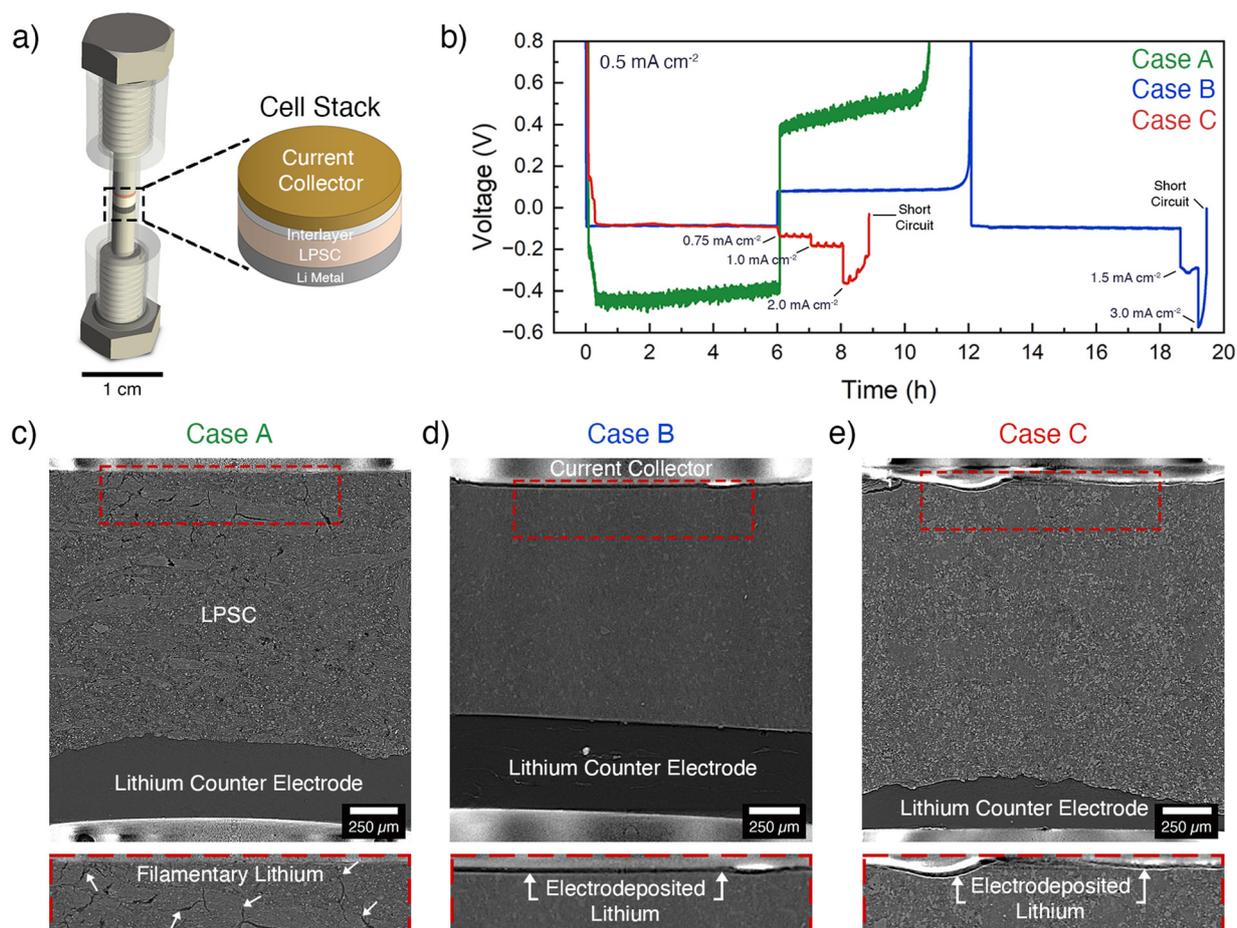

Fig. 1   (a) Schematic of the custom-built tomography cell and cell stack. (b) Voltage curves during galvanostatic deposition/stripping of lithium in three different anode-free cells with lithium counter electrodes (cases A, B, and C) using interlayer-coated Cu current collectors. All three cells were cycled using an initial current density of 0.5 mA cm^{-2} and an areal capacity of 3 mAh cm^{-2} for the first lithium deposition, followed by different treatments (see text). (c–e) Reconstructed image slices of the full cell stacks with magnified interfaces below each stack image. These image slices are from after the initial 3 mAh cm^{-2} was deposited at the current collector. (c) Case A (Au-coated current collector); (d) case B (Ag-coated current collector); (e) case C (Au-coated current collector).

After deposition, lithium was then stripped in case A using a current density of 0.5 mA cm^{-2}, with a dealloying feature observed at ~0.85 V after lithium removal. Although 3 mAh cm^{-2} of lithium was deposited, only 2.4 mAh cm^{-2} was stripped in case A, resulting in a first-cycle CE of 79.9%. A relatively large voltage of about −0.45 V was present during the initial deposition, with the magnitude of the cell voltage decreasing with continued deposition. LPSC with larger particle size was used here compared to cases B and C, which resulted in greater porosity and microstructural heterogeneity in the SSE pellet (see Fig. S1), which likely contributed to the relatively high cell voltage and increased noise in the data. This increased porosity also likely affects the initial uniformity at the current collector|SSE interface, impacting lithium growth dynamics. Despite the unfavorable electrochemical behavior, this cell did not experience a short circuit.

For the cell labeled case B, lithium was deposited, stripped, and re-deposited at 0.5 mA cm^{-2} current density. The absence of a nucleation overpotential at the beginning of lithium deposition is due to the presence of the thin Ag layer used in this cell, which does not feature a distinct plateau since it forms a solid solution with lithium.[12] Throughout the experiment, the cell exhibited a flat voltage profile with relatively low voltage (±0.1 V), suggesting stable deposition and stripping. The first-cycle CE was 92.9%. After the three half-cycles, higher current densities were applied during the second deposition to intentionally cause filamentary growth of lithium. The current density was first increased to 1.5 mA cm^{-2} for a capacity of 0.75 mAh cm^{-2} and then to 3.0 mA cm^{-2} for a capacity of 0.81 mAh cm^{-2}. The cell showed a rapid decrease in the magnitude of the voltage at this highest current density and then short circuited. The observed decrease in voltage is likely attributed to a reduced distance between the counter electrode and lithium growing as filaments prior to short-circuiting.[30] We note that our previous study included data from a single tomographic scan from this same cell,[12] while the current work analyzes the dynamic evolution of this cell over time (many more tomographic scans).

In case C, lithium was first deposited using a current density of 0.5 mA cm^{-2} for 3 mAh cm^{-2}, with the voltage profile being very similar to that in case B, highlighting the reproducibility and stability of these cells. In this cell, a clear alloying plateau was observed above 0 V at the onset of deposition, indicating the alloying of lithium with the Au interlayer prior to lithium deposition. After the first deposition process, the current density was sequentially increased to 0.75 mA cm^{-2}, 1.0 mA cm^{-2}, and 2.0 mA cm^{-2}. At a current density of 2.0 mA cm^{-2}, the voltage profile sloped towards zero until short circuiting after depositing a total areal capacity of 6.37 mAh cm^{-2}, similar to case B.

Fig. 1c–e show reconstructed image slices taken from tomographic scans at the end of the first deposition (*i.e.*, after 3 mAh cm^{-2} of lithium had been deposited) for cases A, B, and C, respectively. The images show the whole cell stack, with the current collectors visible at the top and bottom, the SSE in the middle, and the lithium counter electrode below it. Contrast in

the tomographic image slices arises from the differences in X-ray attenuation coefficients of the materials.[49] The lithium metal counter electrode is darker than the LPSC and steel rods because of the low atomic number of lithium.

Case A (Fig. 1c) shows that the lithium has grown into the SSE as filaments, as indicated by the arrows in the magnified view. In contrast, case B (Fig. 1d) shows an electrodeposited lithium layer with relatively uniform thickness at the working electrode at the top of the image, with no observable lithium within the SSE, which is compact and dense. Case C (Fig. 1e) also featured a uniform lithium layer grown at the working electrode surface without obvious filamentary growth, despite the current collector not being flat (this arose from the intrinsic difficulty of assembling small-diameter tomography cells). Similar to case B, the pelletized SSE in case C is compact with little porosity, likely enabling uniform contact at the current collector|SSE interface despite the non-planar nature of the working electrode. With these results in mind, the different lithium growth and stripping behaviors within these three cells are further explored in the following sections.

Case A: filamentary growth

Case A shows the evolution of lithium in a half cell with a Au-coated Cu current collector and coarse-grained LPSC SSE with higher resistance compared to cases B and C (Fig. 1b). *Operando* imaging was carried out as lithium was deposited and stripped at a current density of 0.5 mA cm^{-2} (Video S1), with the cell showing much higher polarization than the other two cases (Fig. 1b shows electrochemistry). Image segmentation of a subvolume of the SSE near the working electrode current collector was employed to classify various phases (LPSC, lithium, and voids/porosity) based on the grayscale intensity and location of voxels (see SI for methods; Fig. S1 shows the region containing the subvolume). Fig. 2a shows a three-dimensional rendering of the subvolume that shows the segmented porosity within the pristine SSE prior to deposition. The light gray porosity is distributed throughout the subvolume, with some pores existing at the borders of larger LPSC particles. The initial pore volume was measured to be 80×10^4 μm^3 in this subvolume (0.55% of the total volume).

The deposition of lithium in the case A cell primarily involved growth of filaments throughout the SSE rather than at the solid–solid interface. Video S1 shows the evolution of filamentary lithium in case A, showing that lithium filaments grew during deposition and receded upon stripping across the entire subvolume. After depositing 3 mAh cm^{-2} of lithium, extensive cracks within the subvolume had formed to accommodate the filamentary lithium, as shown by the dark gray segmented crack features in Fig. 2b. The original pore volume is also included in light gray within the rendering in Fig. 2b. Most of the newly formed filamentary cracks in Fig. 2b appear to be planar with seemingly random distribution throughout the subvolume.

Fig. 2c presents a series of reconstructed image slices tracking the growth of lithium within a plane extending from near the current collector interface into the SSE (green outline in
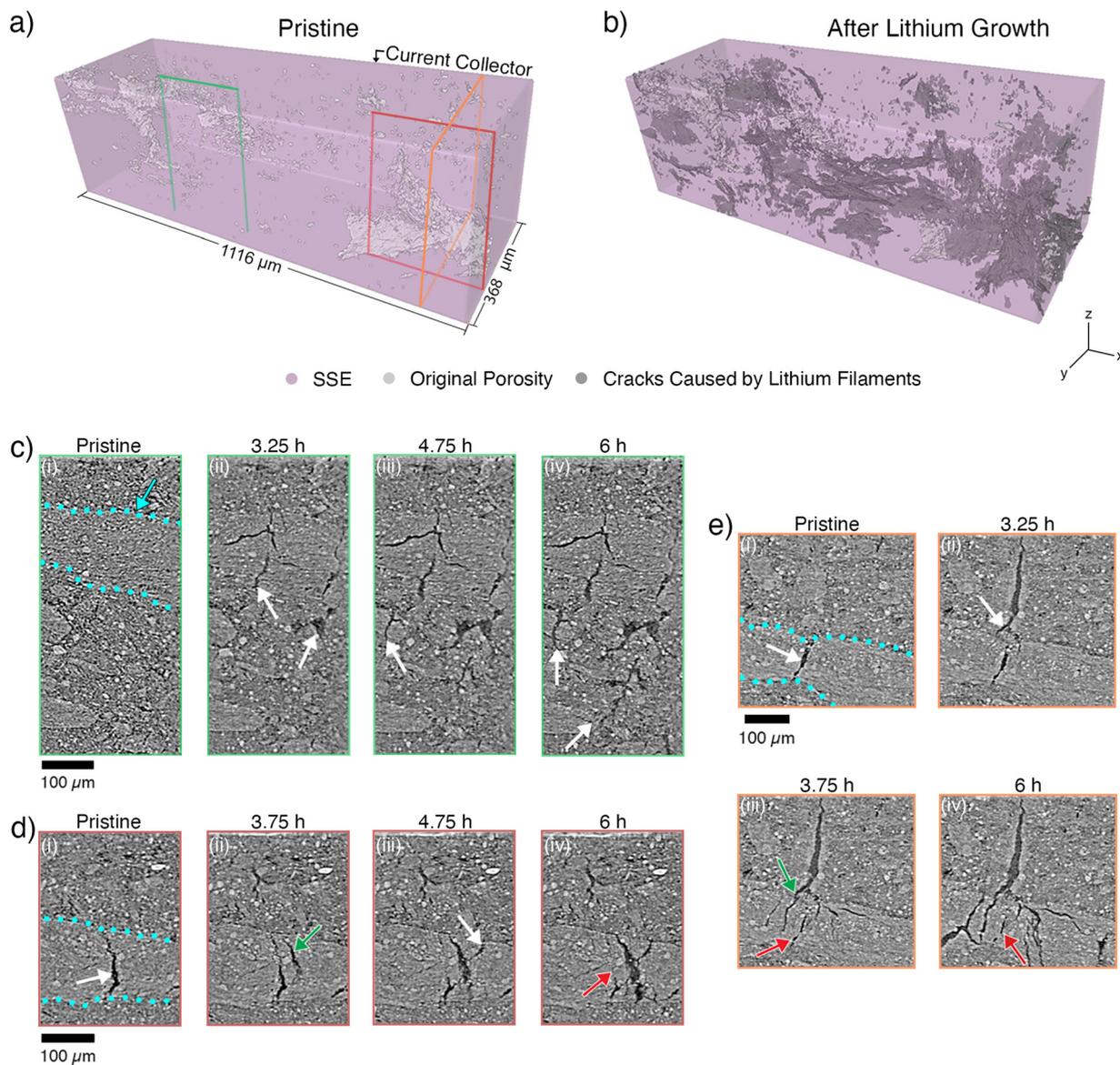
Fig. 2 Filament-driven crack growth during deposition in case A. (a and b) 3D rendering of the analyzed subvolume near the working electrode current collector (a) before any lithium deposition and (b) after 3.0 mAh cm^{-2} of deposition. The top surface of the 3D rendering is the current collector|SSE interface, and the lithium counter electrode is located well below the reconstructed volume. (c–e) Reconstructed image slices taken from tomographic scans during deposition for case A from three different locations. The location of each image slice within the subvolume is shown in (a) with the green, red, and orange outlines indicating the locations of c, d, and e, respectively. The current collector|SSE interface is at the top of these images.

Fig. 2a). Prior to deposition (i), relatively large SSE particles are visible with a particularly large particle outlined in blue traversing the width of the image. As lithium filaments grew into the SSE toward the counter electrode below the image frame, new cracks formed within this large particle, as denoted by the white arrows in (ii). Continued deposition extended the cracks within this large particle, with cracks beginning to grow below the particle as well, growing through another LPSC particle in frame (iii) (see arrow). The thin branched tip continued to grow down towards the counter electrode, and by the end of deposition (iv), several branched crack networks had fully tra-

versed this image frame, although they had not reached the counter electrode to short circuit the cell.

While the spatial distribution of lithium metal within these cracks was not able to be accurately analyzed due to overlap of the grayscale intensity distribution of lithium and pores (see subsequent discussion), we note that the branching dendritic structure of the cracks in Fig. 2c(iii and iv) may suggest that lithium was present near the crack tips, since the branching could be driven by lithium growth in different directions. Furthermore, the cracks were observed to initially widen and then stabilize over one or two image frames, indicating that

the already-formed cracks did not further widen while they continue to grow toward the counter electrode.

Fig. 2d shows the fracture process in another plane within this subvolume (red outline in Fig. 2a). In the pristine state (Fig. 2d(i)), an empty crack was present within the large SSE particle (blue outline, white arrow). This is the same large particle as observed in Fig. 2c. During lithium deposition (Fig. 2d (ii)), new cracks formed above and within the large particle as lithium grew from the working electrode. Interestingly, this new crack (green arrow in Fig. 2d(ii)) formed next to the pre-existing crack, closing the upper part of the pre-existing crack as lithium growth expanded the new adjacent crack. Continued lithium deposition resulted in additional growth of filament-induced cracks in Fig. 2d(iii), and by frame (iv), the original crack was almost fully closed (red arrow), indicating that it was not filled with lithium. These observations show that lithium does not necessarily fill pre-existing porosity within the SSE and can instead form new cracks that cause pre-existing pores to close. This does not preclude the growth of lithium into pre-existing porosity, but it does highlight the presence of complex growth behavior. Furthermore, we note that the large filament-induced crack continued growing in width in frames (ii)–(iv) even as it also extended toward the counter electrode.

Fig. 2e captures the evolution of lithium filaments in an image slice that is in a different plane within the subvolume (orange outline in Fig. 2a). Video S2 shows the lithium growth and stripping behavior at this plane, in which similar growth dynamics were observed as the previous case. As lithium grew in Fig. 2e, a large lithium filament (white arrow in Fig. 2e(ii)) extended from the working electrode above the image frame down towards the large LPSC particle (outlined in blue in Fig. 2e(i)). When the filament reached the large particle (Fig. 2e(iii)), the single crack branched into new cracks (green arrow) and began growing around a pre-existing pore (red arrow). By the end of deposition, a network of new cracks was observed within the large LPSC particle which forced the original pore to close (Fig. 2e(iv), red arrow). These observations show that lithium likely fills this large crack and the branching cracks as they grow rather than filling the initial empty pore volume in the SSE.

After 3.0 mAh cm^{-2} of lithium growth in this cell, the cell had not yet short-circuited, and the current was reversed to cause lithium stripping. The images snapshots in Fig. 3a and b track the stripping of the lithium within regions previously presented in Fig. 2c and e, respectively. In Fig. 3a(i and ii), the tips of the filaments furthest away from the current collector were observed to undergo stripping first, and they shrunk as lithium was removed. This reversible filamentary plating and stripping behavior is consistent with previous observations from *operando* optical microscopy.[30] The stripping process visibly moved up along the cracks toward the current collector as time proceeded, with the cracks shrinking in volume (this is quantified subsequently). Some lithium-filled cracks became thinner over time without fully closing (Fig. 3a(iii)–(v)). The same behavior was observed for the lithium-filled cracks in

Fig. 3b, as shown in Video S2. The lithium stripping process in Fig. 3b left behind an array of damage and crack remnants, including new cracks that formed during shrinkage of the lithium-filled cracks presumably due to adhesion between lithium and the LPSC crack wall (see green arrows in Fig. 3b(ii and iii)).

Fig. S2 shows the segmented 3D subvolume after stripping, with both the original porosity and new cracks introduced by filamentary growth and stripping visible. This can be compared to the same subvolume after deposition in Fig. 2b. Furthermore, Video S3 dynamically tracks crack growth and shrinkage within the entire subvolume, distinguishing between pre-existing cracks and cracks induced by lithium growth.

To further analyze the evolution of cracks in case A, the total pore and crack volume over time was quantified within a larger subvolume that encompasses the subvolume in Fig. 2a, b and extends down to the lithium counter electrode (see Fig. S1). Fig. 3c is a plot of the total pore and crack volume as a function of time, along with the electrochemical curve for case A above the plot. This volume includes porosity in the initial pellet as well as the additional crack volume induced by lithium growth and stripping within the SSE. The measured volume remains relatively constant over the first 2 h of deposition (corresponding to ~1 mAh cm^{-2} of deposited lithium), and the voltage profile is also constant. After this, the volume begins to steadily increase until the end of deposition, along with decreasing polarization of the cell. The initial period of constant volume is likely because lithium is growing at the current collector|SSE interface, but it is too thin to clearly be resolved with X-ray µCT due to the high contrast at the interface between the current collector and SSE. Indeed, Video S1 shows evidence for some lithium formation at the interface before crack growth, with a thin darker layer growing at the interface. Over the remaining 4 h of deposition, the pore + crack volume within the subvolume increased from 266×10^4 µm^3 to 461×10^4 µm$_3$, representing 195×10^4 µm^3 or a 73% increase of new crack volume. Assuming uniform distribution of lithium growth across the entire electrode area, deposition of this amount of lithium (2.0 mAh cm^{-2}) would theoretically correspond to 398×10^4 µm^3 of new lithium within this subvolume. Thus, the measured cracks formed in this subvolume can accommodate 49% of the total deposited lithium. The remaining lithium may be depositing (i) into the extensive pre-existing porosity in this subvolume, (ii) into cracks too small to be resolved, (iii) at the current collector interface, and/or (iv) non-uniformly outside of this subvolume.

After 6 h of deposition, the current was reversed and the lithium was stripped from the working electrode. As seen in Fig. 3a and b, lithium was removed from the cracks to cause them to shrink, and the total pore + crack volume was observed to linearly decrease with time during stripping (Fig. 3c). After about 2.25 h of stripping, the pore + crack volume reached a plateau despite continued stripping from the working electrode, suggesting that all accessible lithium was removed from the cracks and the lithium at the interface
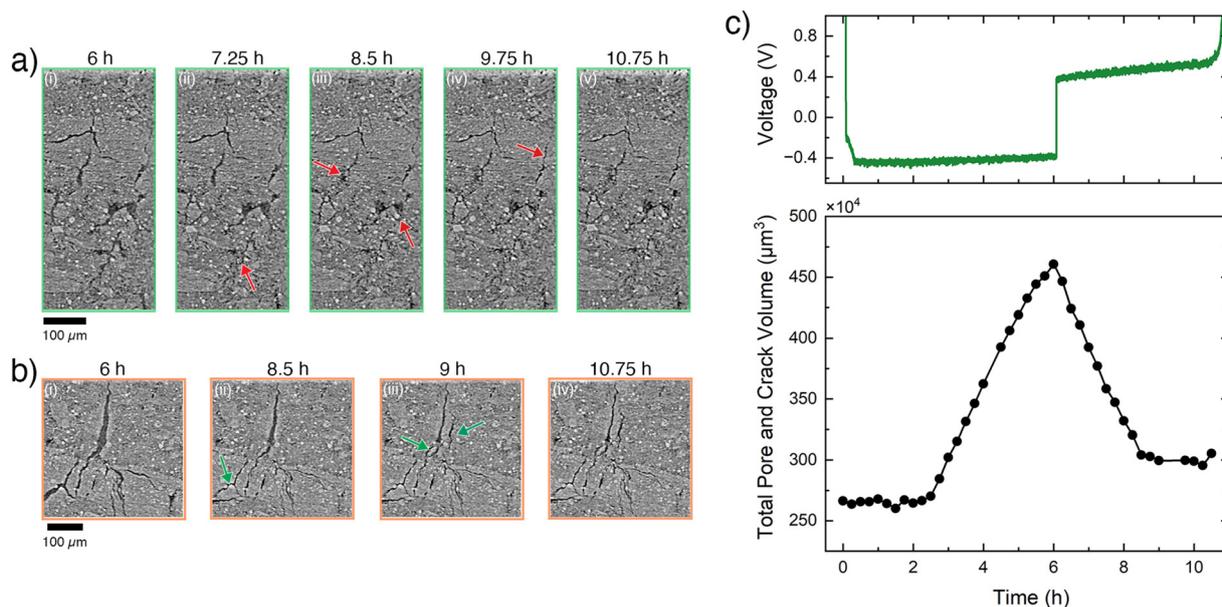
Fig. 3 Lithium stripping in case A. (a and b) Reconstructed image slices taken from tomographic scans during stripping from the locations shown in Fig. 2c and e, respectively. Red arrows show points where lithium recedes during stripping. Green arrows denote new cracks that form during stripping due to closure of the lithium-filled cracks. (c) The segmented total pore and crack volume within the SSE plotted as a function of time for the larger subvolume denoted in Fig. S1 (green outline), with the galvanostatic curve for reference above. The total pore and crack volume includes both the porosity in the initial pellet and the additional crack volume caused during lithium growth and stripping within the SSE.

or other pore regions was stripped during the remaining time. The total pore + crack volume at the end of the experiment was greater than the original pore + crack volume in the pristine SSE despite shrinking of the cracks during lithium stripping. Since this cell only exhibited 80% CE, this increase in crack volume from the start to the end could be due to inactive lithium within the cracks that cannot be accessed due to loss of electrical contact to the working electrode current collector. New cracks that formed during the stripping of lithium-filled cracks due to the adhesion between lithium and SSE crack wall (see Fig. 3b) may also contribute to the higher crack volume after stripping. Overall, these data show that while lithium is stripped from the lithium-filled cracks, there is a fundamental irreversibility in which some of the damage remains at the end of the full cycle (Fig. S2).

We also investigated the possibility of grayscale pixel intensity-based segmentation of lithium metal from unfilled void space within SSE cracks, as has been reported in other works.[42,43,50,51] Grayscale intensities were extracted from line scans of pores/cracks with known lithium content (e.g., empty pores in the pristine SSE vs. filled cracks after lithium growth) at different stages of the filament growth process (Fig. S3). The grayscale intensity histograms of the empty pores and the lithium-filled cracks exhibit two different approximate normal distributions (Fig. S4), but the distributions overlap. The wider intensity distribution of the empty pores is because these were generally smaller, and contrast bleeding at the edge of the cracks may contribute. Although there are distinct average grayscale intensity values for lithium-filled cracks and empty pores, the significant overlap of the histograms in this case

prevented accurate automated segmentation of empty pores vs. filled cracks within the SSE.

To provide information on reproducibility of similar cells, two similar anode-free half cells with the same coarse-grained LPSC were imaged before and after lithium deposition at a current density of 0.5 mA cm^{-2} and compared to case A (Fig. S5). Among the three coarse-grained cells, each exhibited variations in cell voltage during deposition, and differences of the SSE porosity were also observed. These observations highlight the challenges of controlling packing density in SSEs with larger and more variable particle sizes, which likely contributes to the variability in electrochemical behavior. Despite these differences, however, filamentary lithium growth across the entire electrode interface was observed in all three cells instead of the deposition of a flat lithium layer, indicating reproducibility of the morphology evolution amongst our experiments when using this type of SSE.

Case B: uniform growth

As previously introduced, the cell in case B exhibits relatively uniform lithium growth at the current collector interface, and the fine-grained SSE in case B was denser than case A with little observed porosity (Fig. 1d). Fig. 4 shows a portion of a reconstructed image slice from case B at different times during cycling. This image set shows the Ag-coated current collector|SSE interface at the same position over the course of the experiment, and Video S4 shows the entire cell cross section and its evolution across 40 tomographic scans throughout the experiment. Prior to lithium deposition at the working electrode current collector (Fig. 4a), uniform interfacial contact
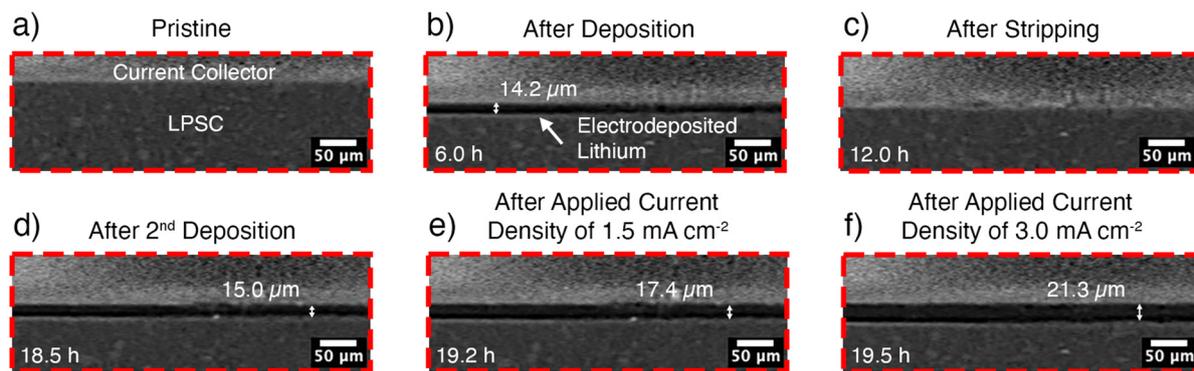
Fig. 4 Reconstructed image slices taken from tomographic scans of the cell denoted as case B showing the interface between the working electrode ("Current Collector") and the LPSC at various stages of cycling. (a) The pristine state before cycling. (b) After 3.0 mAh cm^{-2} of lithium was deposited on the working electrode. (c) After 2.8 mAh cm^{-2} of lithium was stripped. (d) After re-deposition of 3.0 mAh cm^{-2} of lithium. (e) After increasing the current density to 1.5 mA cm^{-2} and depositing 0.80 mAh cm^{-2} of lithium. (f) After further increasing the current density to 3.0 mA cm^{-2} and depositing 0.80 mAh cm^{-2}, at which point the cell short-circuited.

was observed between the current collector and the SSE. After the first lithium deposition step (Fig. 4b), a lithium layer measuring an average thickness of 14.2 μm ± 2.4 μm was present, resulting in two distinct interfaces (SSE|lithium and lithium|current collector). This thickness value, measured over a ~1.5 mm diameter region, is close to the theoretically expected thickness of 14.5 μm for 3.0 mAh cm^{-2} of deposited lithium.

At the end of the first stripping step (Fig. 4c), lithium was removed from the interface, resulting in reestablishment of contact between the current collector and SSE. However, some wrinkling and possible damage are observed at the interface as compared to the pristine interface (Fig. 4a). With a 92.9% first-cycle CE, there is likely some inactive lithium left at the interface that contributes to the interfacial wrinkles. The observed wrinkle-like contrast could also be due to particulate Ag-alloy interlayer material present at the end of stripping.[12,52]

After the second lithium deposition step (*i.e.*, the third half-cycle), lithium was again visible at the interface with an average thickness of 15.0 μm ± 2.6 μm (Fig. 4d), as measured over the wider interface area. Since ~0.2 mAh cm^{-2} (~1 μm) of lithium remained from the previous half-cycle, this increase in average thickness may be due to the residual lithium at the interface. After three half-cycles, the current density was tripled to 1.5 mA cm^{-2} to purposely induce filamentary growth. After depositing an additional 0.80 mAh cm^{-2}, the lithium layer continued to grow, with the average thickness increasing to 17.4 μm ± 2.8 μm. The current density was then increased to 3.0 mA cm^{-2}, which caused short circuiting (see galvanostatic curve in Fig. 1b) due to a filament growing through the SSE outside of the image frame in Fig. 4. The lithium layer grew to an average thickness of 21.3 μm ± 3.3 μm by the time the short circuit occurred.

The images in Fig. 4 show that within a single visualized slice of the interface, the lithium retained relatively uniform thickness during the multiple electrochemical growth and

stripping processes. To further quantify lithium thickness evolution across a much greater area of the interface, image segmentation was carried out. The electrodeposited lithium volume at the working electrode and the lithium volume at the counter electrode were both segmented and tracked over time. We segmented ~75% of the total electrode area at the center of the cell (a diameter of ~1.5 mm), since segmentation of the cell edges is less accurate due to varying voxel intensity near the edges of the PEEK and metal rods. We note that this analysis was used to extract the average thickness values quoted previously. The high grayscale pixel intensity of the stainless-steel rod and Cu current collector makes it difficult to accurately separate the low-intensity lithium from the rod when it is thin at the early stages of deposition; thus, we analyzed the electrodeposited layer after a sufficiently thick (~10 μm thick) lithium layer was deposited. Despite this limitation, this analysis provides useful information about material dynamics within the cell.

The galvanostatic curve for case B is shown in Fig. 5a, along with the evolution of average lithium thickness of the working electrode and the average thickness change of the counter electrode (Fig. 5b). The evolution of the average thickness followed an expected linear trend over the first three half-cycles at 0.5 mA cm^{-2} current density. As expected, the counter electrode thickness decreased during the first half-cycle, increased during the second, and once again decreased in the third half-cycle. The Ag-coated Cu working electrode thickness exhibited the opposite behavior, although the segmentation was only performed when the lithium at the working electrode was thick enough. The standard deviation of these measured average thicknesses (Fig. 5c) remained fairly constant for both electrodes over the first three half-cycles, indicating that the lithium thickness was relatively uniform across the cell during these processes.

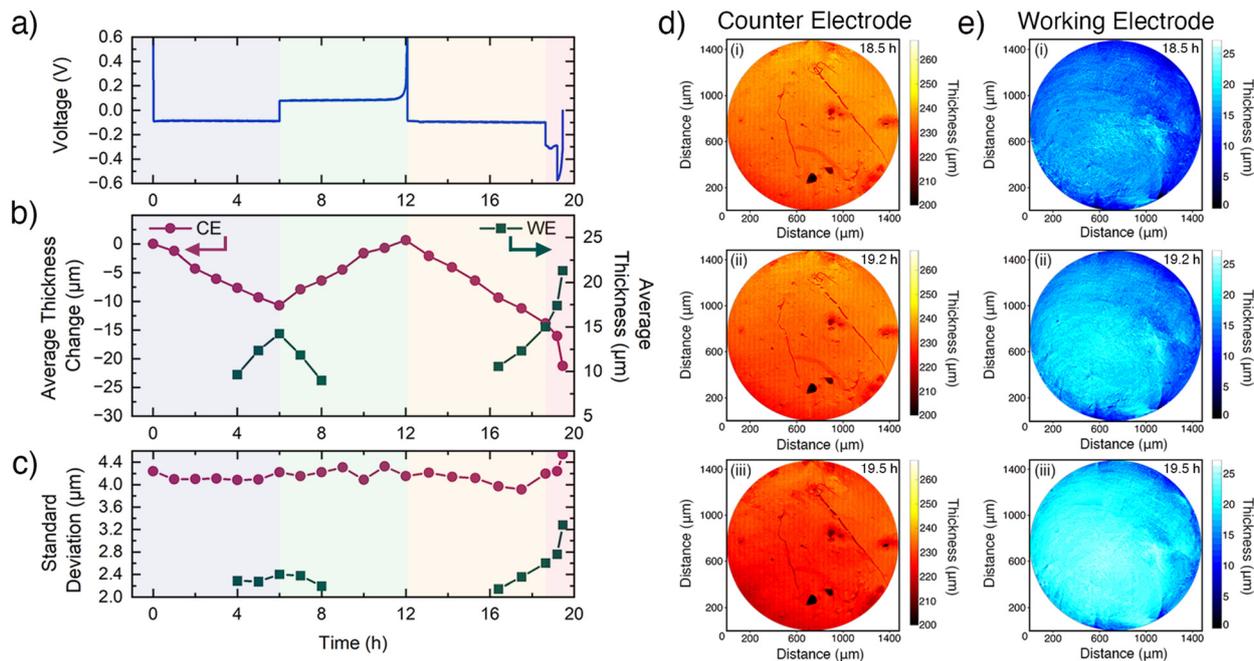As lithium was plated and stripped, there were differences in the measured thicknesses of lithium at the working and

Fig. 5 Segmentation analysis of lithium evolution for case B. (a) Electrochemical curve, (b) average thickness over time for the working electrode (right axis) and average thickness change for the counter electrode (left axis), and (c) the standard deviation of the average thickness for the working and counter electrodes. (d and e) Thickness maps showing the lithium thickness across the segmented area of the interface for the counter electrode (d) and working electrode (e) at (i) the end of the third half-cycle, (ii) after holding at 1.5 mA cm^{-2}, and (iii) after holding at 3.0 mA cm^{-2}. Thickness maps were generated by summing the entire lithium thickness at each position across the interface at both electrodes.

counter electrodes. After the first half-cycle, the average thickness of the lithium at the counter electrode decreased by ~11 μm, while the deposited layer at the working electrode was ~14 μm thick (Fig. 5b). The difference of average thickness change between the two electrodes likely arises because the lithium at the edges of the cell was not able to be reliably tracked in this analysis (only ~75% of the electrode area was segmented). The smaller thickness change at the counter electrode compared to the working electrode suggests that excess lithium was preferentially deposited and stripped at the edges of the counter electrode outside of the area of analysis.

By the end of the third half-cycle, a uniform lithium layer was redeposited (Fig. 4d) and the current density was then increased to intentionally induce filament growth. Fig. 5b shows that the average thickness changed more rapidly at these higher current densities. Notably, the standard deviation of the thickness increased at the higher current densities before short circuiting (Fig. 5c), especially for the working electrode. This increase of standard deviation suggests that there is greater thickness nonuniformity over the working electrode at the higher current densities. Such thickness nonuniformity is associated with greater variation of current density across the interface, which would increase the probability of filament initiation at a defect or flaw.

Fig. 5d and e contains maps showing the spatial variation of lithium thickness at the counter electrode (Fig. 5d) and working electrode (Fig. 5e) near the end of the experiment. These maps show the lithium thickness represented by color

intensity at each position across the interface at three different times as lithium is deposited at the working electrode. The maps are shown at the end of the third half-cycle (i), as well as after holding at current densities of 1.5 mA cm^{-2} (ii) and 3.0 mA cm^{-2} (iii). Interfacial nonuniformities and defects are apparent, especially at the counter electrode (Fig. 5d). The counter electrode has linear divots across the interface, which were likely introduced during assembly, as well as particulate-shaped indentations in the metal due to stray LPSC particles. These defects were present in the pristine state and were not formed during the electrochemical experiment (Fig. S6). Despite these defects, lithium was stripped and deposited relatively uniformly at the counter electrode. The deposited lithium layer at the working electrode has fewer visible defects present and appears to be more uniform (Fig. 5e).

Subtle variations of lithium thickness are evident across the working electrode interface (Fig. 5e). After the third half-cycle (Fig. 5e(i)), the deposited lithium at the working electrode was relatively uniform in thickness, with regions of thinner lithium visible around the edges. After deposition at higher current densities (Fig. 5e(ii and iii)), the lithium thickness increased across the electrode surface but with greater thickness in the middle of the cell. The variation of thickness could be due to nonuniform stack pressure across the cell or slight misalignment of cell fixtures. Interestingly, at the higher current densities, lithium was deposited on the planar layer without filament growth within this central region covering 75% of the interfacial area, while fracture and filament
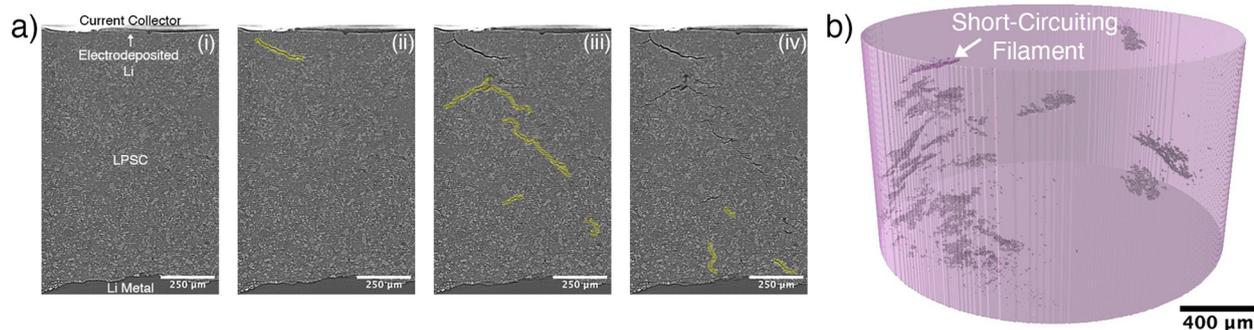
Fig. 6 Lithium filament growth in case C. (a) Tomographic images after (i) 3.0 mAh cm^{-2} of deposition at 0.5 mA cm^{-2}, (ii) after an additional 0.75 mAh cm^{-2} of deposition at 0.75 mA cm^{-2}, (iii) after an additional 1.0 mAh cm^{-2} deposition at 1.0 mA cm^{-2}, and (iv) after additional deposition at 2.0 mA cm^{-2}. New filaments within the SSE in each image frame are highlighted in yellow. (b) Three-dimensional rendering of the segmented SSE after cell failure. The lithium filament network (gray) is evident within the SSE volume (purple).

initiation was observed at the edges of the cell (Fig. S7 and Video S4). Such edge effects may be caused by a different chemo-mechanical environment or SSE density due to the influence of the cell walls and current collector edges.

To summarize the behavior of the cell in case B, the *operando* X-ray μCT results showed that lithium deposited and stripped as a relatively uniform layer at low current densities, which is important for achieving high CE and long cycle life of anode-free SSBs. The compact nature and relatively small particle size of the LPSC SSE used here may have enabled good initial contact at the solid–solid interface and low interfacial resistance at the Ag-coated Cu current collector interface, promoting uniform growth. The segmentation analysis showed an average roughening of the working electrode surface during the filament initiation process before short circuiting, suggesting that variation in local current density is related to an increased probability for filament initiation.

Case C: filament growth after initial planar deposition

For comparison to cases A and B, case C involved tracking lithium growth at increasing current densities without stripping. For case C, a uniform lithium layer was first deposited without imaging in a half-cell on an Au-coated current collector using fine-grained LPSC with similar resistance and SSE porosity to case B (Fig. S8). This cell exhibited relatively low cell voltage (Fig. 1b), and a lithium layer of relatively uniform thickness was first formed at the current collector|SSE interface after 3.0 mAh cm^{-2} of electrodeposition at 0.5 mA cm^{-2} (Fig. 6a). After this process, the current density was incrementally increased to induce short circuiting while *operando* imaging was carried out, as shown in Video S5. Increasing the current density to 0.75 mA cm^{-2} and then to 1.0 mA cm^{-2} caused thicker lithium growth at the interface while a lithium filament also nucleated and grew across the cell. The filament contacted the counter electrode and short circuited the cell after the current density was increased to and held at 2.0 mA cm^{-2}; the voltage also decreased during filament growth. The filament progression across the cell is captured in the image slices in Fig. 6.

Fig. 6b shows a three-dimensional rendering of the SSE and the filamentary cracks captured within the cell. The crack grew in a branching fashion, with lithium presumably filling most of the various branches. The cracks are located primarily near the edges of the cell, as also seen for case B. Additional cracks around the edges of the cell are significantly smaller and are not the source of cell failure, as they have not transitioned to form filaments that traverse the cell.

Case C tracks the growth evolution of a single filament from an anode-free current collector at heightened current densities, which is a typical form of failure in SSBs.[40–42] The behavior observed in case C is in contrast to case A, where the filamentary growth was much more widespread across the electrode area. The lower resistance, smaller particle size, and higher packing density of the SSE pellets in cases B and C likely contributed to the improved electrochemical behavior and markedly different lithium morphology evolution than in case A. However, it is difficult to delineate the specific contributions that give rise to the differences. Overall, these findings vividly demonstrate the need for realistic cell formats and electrochemical operation (*i.e.*, low polarization) *in operando* experiments.

Conclusions

In this work, *operando* X-ray μCT and image segmentation have been used to uncover diverse lithium growth dynamics at the microscale in three different anode-free SSB cells. In one cell with high resistance, we observed extensive crack formation across the entire SSE|electrode interface with complex lithium growth behavior, with some lithium-filled cracks growing around and closing existing empty pores, rather than lithium growing directly in the pores. Quantification of the crack volume showed accumulated mechanical damage after the end of a full cycle, indicating that trapped lithium was present. In a different cell with lower resistance, we showed that lithium can deposit and strip uniformly across the current collector| SSE interface. Image segmentation revealed average roughen-

ing of the lithium at the working electrode at elevated current densities shortly before filament-induced short circuiting. Finally, a cell was investigated that featured low cell resistance but with higher currents causing the growth of a single filament across the cell to form a short circuit.

While several studies have examined lithium filament growth in SSBs, our investigation of diverse fracture and filament growth behavior on alloy-coated current collectors in anode-free cells adds new knowledge of these systems. We explicitly show that filament-driven crack growth is fundamentally different at high and low polarization in different cells at the same current density, with high polarization being associated with extensive filament growth across the entire solid–solid interface, unlike that typically observed in low-resistance cells. Furthermore, our data strongly suggest that in many cases, cracks can be filled with lithium as they grow, as indicated by the observed expansion of cracks closing neighboring porosity, the widening of cracks with time, and the shrinkage of the cracks during removal of lithium. The growth of lithium filaments within the SSE was also found to be partially reversible, but with lithium removal not healing all the mechanical damage.

More work is needed to understand the role of applied stack pressure and global stress state on the overall reversibility of crack growth and shrinkage, as well as efforts to model the complex chemo-mechanical environment that causes filaments and cracks to form in SSEs. Additionally, further investigation into the effects of particle orientation and packing density during the processing of the SSE separator is essential to improve reproducibility and ensure optimal conditions for lithium growth. While our findings are likely applicable to other sulfide-based SSEs, the role of the solid–solid interface and its impact on lithium morphology is critical across all SSE systems. In future work, it would be interesting to explore how the solid–solid interface and SSE porosity influence lithium growth when using oxide and halide SSE materials, as differences in ionic conductivity or interfacial stability may impact lithium evolution. Overall, our findings provide critical insights into the factors governing lithium growth in anode free SSBs, and in particular they emphasize the variety of filament growth/shrinkage processes possible, which must be carefully considered for SSB engineering.

Author contributions

S. E. S.: conceptualization, methodology, software, validation, formal analysis, investigation, writing—original draft, writing —review & editing, visualization, funding acquisition; D. L. N.: software, validation, investigation; H. S.: formal analysis, visualization; T. A. T.: investigation; J. A. L.: investigation; K. A. C.: investigation; P. S.: investigation; N. P. D.: writing—review & editing; F. L. E. U. V.: investigation; D. P. F.: investigation, writing—review & editing; M. T. M.: conceptualization, methodology, writing—original draft, writing—review & editing, supervision, and funding acquisition.

Conflicts of interest

The authors have no conflicts to declare.

Data availability

Supporting data for this article will be made available as SI. Experimental methods; image processing, segmentation, and analysis, supplementary X-ray CT images and analysis, supplementary video captions. See DOI: https://doi.org/10.1039/d5eb00111k.

Acknowledgements

References

1 J. Janek and W. G. Zeier, *Nat. Energy*, 2016, **1**, 16141.
2 B. S. Vishnugopi, E. Kazyak, J. A. Lewis, J. Nanda, M. T. McDowell, N. P. Dasgupta and P. P. Mukherjee, *ACS Energy Lett.*, 2021, **6**, 3734–3749.
3 M. J. Wang, E. Kazyak, N. P. Dasgupta and J. Sakamoto, *Joule*, 2021, **5**, 1371–1390.
4 Y. G. Lee, S. Fujiki, C. Jung, N. Suzuki, N. Yashiro, R. Omoda, D. S. Ko, T. Shiratsuchi, T. Sugimoto, S. Ryu, J. H. Ku, T. Watanabe, Y. Park, Y. Aihara, D. Im and I. T. Han, *Nat. Energy*, 2020, **5**, 299–308.
5 T. Famprikis, P. Canepa, J. A. Dawson, M. S. Islam and C. Masquelier, *Nat. Mater.*, 2019, **18**, 1278–1291.
6 A. Manthiram, X. Yu and S. Wang, *Nat. Rev. Mater.*, 2017, **2**, 16103.
7 E. P. Alsaç, D. L. Nelson, S. G. Yoon, K. A. Cavallaro, C. Wang, S. E. Sandoval, U. D. Eze, W. J. Jeong and M. T. McDowell, *Chem. Rev.*, 2025, **125**, 2009–2119.
8 K. B. Hatzell, X. C. Chen, C. L. Cobb, N. P. Dasgupta, M. B. Dixit, L. E. Marbella, M. T. McDowell,

P. P. Mukherjee, A. Verma, V. Viswanathan, A. S. Westover and W. G. Zeier, *ACS Energy Lett.*, 2020, **5**, 922–934.

9 Y. Shen, Y. Zhang, S. Han, J. Wang, Z. Peng and L. Chen, *Joule*, 2018, **2**, 1674–1689.

10 P. Albertus, S. Babinec, S. Litzelman and A. Newman, *Nat. Energy*, 2018, **3**, 16–21.

11 S. E. Sandoval and M. T. McDowell, *Matter*, 2023, **6**, 2101–2102.

12 S. E. Sandoval, J. A. Lewis, B. S. Vishnugopi, D. L. Nelson, M. M. Schneider, F. J. Q. Cortes, C. M. Matthews, J. Watt, M. Tian, P. Shevchenko, P. P. Mukherjee and M. T. McDowell, *Joule*, 2023, **7**, 2054–2073.

13 J. A. Lewis, S. E. Sandoval, Y. Liu, D. L. Nelson, S. G. Yoon, R. Wang, Y. Zhao, M. Tian, P. Shevchenko, E. Martínez-Pañeda and M. T. McDowell, *Adv. Energy Mater.*, 2023, **13**, 2204186.

14 S. E. Sandoval, C. G. Haslam, B. S. Vishnugopi, D. W. Liao, J. S. Yoon, S. H. Park, Y. Wang, D. Mitlin, K. B. Hatzell, D. J. Siegel, P. P. Mukherjee, N. P. Dasgupta, J. Sakamoto and M. T. McDowell, *Nat. Mater.*, 2025, **24**, 673–681.

15 A. L. Davis, E. Kazyak, D. W. Liao, K. N. Wood and N. P. Dasgupta, *J. Electrochem. Soc.*, 2021, **168**, 070557.

16 K. Lee and J. Sakamoto, *Adv. Energy Mater.*, 2024, **14**, 2303571.

17 C. Haslam and J. Sakamoto, *J. Electrochem. Soc.*, 2023, **170**, 040524.

18 M. J. Wang, E. Carmona, A. Gupta, P. Albertus and J. Sakamoto, *Nat. Commun.*, 2020, **11**, 5201.

19 T. Krauskopf, F. H. Richter, W. G. Zeier and J. Janek, *Chem. Rev.*, 2020, **120**, 7745–7794.

20 D. K. Singh, A. Henss, B. Mogwitz, A. Gautam, J. Horn, T. Krauskopf, S. Burkhardt, J. Sann, F. H. Richter and J. Janek, *Cell Rep. Phys. Sci.*, 2022, **3**, 101043.

21 V. Raj, V. Venturi, V. R. Kankanallu, B. Kuiri, V. Viswanathan and N. P. B. Aetukuri, *Nat. Mater.*, 2022, **21**, 1050–1056.

22 J. A. Lewis, F. J. Q. Cortes, Y. Liu, J. C. Miers, A. Verma, B. S. Vishnugopi, J. Tippens, D. Prakash, T. S. Marchese, S. Y. Han, C. Lee, P. P. Shetty, H. W. Lee, P. Shevchenko, F. De Carlo, C. Saldana, P. P. Mukherjee and M. T. McDowell, *Nat. Mater.*, 2021, **20**, 503–510.

23 J. Kasemchainan, S. Zekoll, D. Spencer-Jolly, Z. Ning, G. O. Hartley, J. Marrow and P. G. Bruce, *Nat. Mater.*, 2019, **18**, 1105–1111.

24 M. J. Wang, R. Choudhury and J. Sakamoto, *Joule*, 2019, **3**, 2165–2178.

25 F. Shen, M. B. Dixit, X. Xiao and K. B. Hatzell, *ACS Energy Lett.*, 2018, **3**, 1056–1061.

26 K. Lee, E. Kazyak, M. J. Wang, N. P. Dasgupta and J. Sakamoto, *Joule*, 2022, **6**, 2547–2565.

27 L. Porz, T. Swamy, B. W. Sheldon, D. Rettenwander, T. Frömling, H. L. Thaman, S. Berendts, R. Uecker, W. C. Carter and Y. M. Chiang, *Adv. Energy Mater.*, 2017, **7**, 1701003.

28 F. Han, A. S. Westover, J. Yue, X. Fan, F. Wang, M. Chi, D. N. Leonard, N. J. Dudney, H. Wang and C. Wang, *Nat. Energy*, 2019, **4**, 187–196.

29 B. S. Vishnugopi, M. B. Dixit, F. Hao, B. Shyam, J. B. Cook, K. B. Hatzell and P. P. Mukherjee, *Adv. Energy Mater.*, 2022, **12**, 2102825.

30 E. Kazyak, R. Garcia-Mendez, W. S. LePage, A. Sharafi, A. L. Davis, A. J. Sanchez, K. H. Chen, C. Haslam, J. Sakamoto and N. P. Dasgupta, *Matter*, 2020, **2**, 1025–1048.

31 E. Kazyak, M. J. Wang, K. Lee, S. Yadavalli, A. J. Sanchez, M. D. Thouless, J. Sakamoto and N. P. Dasgupta, *Matter*, 2022, **5**, 3912–3934.

32 M. Sun, T. Liu, Y. Yuan, M. Ling, N. Xu, Y. Liu, L. Yan, H. Li, C. Liu, Y. Lu, Y. Shi, Y. He, Y. Guo, X. Tao, C. Liang and J. Lu, *ACS Energy Lett.*, 2021, **6**, 451–458.

33 Y. Lu, C.-Z. Zhao, J.-K. Hu, S. Sun, H. Yuan, Z.-H. Fu, X. Chen, J.-Q. Huang, M. Ouyang and Q. Zhang, *Sci. Adv.*, 2022, **8**, 510.

34 J. Su, M. Pasta, Z. Ning, X. Gao, P. G. Bruce and C. R. M. Grovenor, *Energy Environ. Sci.*, 2022, **15**, 3805–3814.

35 M. Siniscalchi, J. Liu, J. S. Gibson, S. J. Turrell, J. Aspinall, R. S. Weatherup, M. Pasta, S. C. Speller and C. R. M. Grovenor, *ACS Energy Lett.*, 2022, **7**, 3593–3599.

36 Y. Chen, Z. Wang, X. Li, X. Yao, C. Wang, Y. Li, W. Xue, D. Yu, S. Y. Kim, F. Yang, A. Kushima, G. Zhang, H. Huang, N. Wu, Y. W. Mai, J. B. Goodenough and J. Li, *Nature*, 2020, **578**, 251–255.

37 X. Lu, Y. Cheng, M. Li, Y. Zou, C. Zhen, D. Wu, X. Wei, X. Li, X. Yang and M. Gu, *Adv. Funct. Mater.*, 2023, **33**, 2212847.

38 Z. Wang, J. Zhao, X. Zhang, Z. Rong, Y. Tang, X. Liu, L. Zhu, L. Zhang and J. Huang, *eScience*, 2023, **3**, 100087.

39 D. L. Nelson, S. E. Sandoval, J. Pyo, D. Bistri, T. A. Thomas, K. A. Cavallaro, J. A. Lewis, A. S. Iyer, P. Shevchenko, C. V. Di Leo and M. T. McDowell, *ACS Energy Lett.*, 2024, **9**, 6085–6095.

40 D. Spencer-Jolly, Z. Ning, G. O. Hartley, B. Liu, D. L. R. Melvin, P. Adamson, J. Marrow and P. G. Bruce, *ACS Appl. Mater. Interfaces*, 2021, **13**, 22708–22716.

41 J. M. Doux, H. Nguyen, D. H. S. Tan, A. Banerjee, X. Wang, E. A. Wu, C. Jo, H. Yang and Y. S. Meng, *Adv. Energy Mater.*, 2020, **10**, 1903253.

42 Z. Ning, D. S. Jolly, G. Li, R. De Meyere, S. D. Pu, Y. Chen, J. Kasemchainan, J. Ihli, C. Gong, B. Liu, D. L. R. Melvin, A. Bonnin, O. Magdysyuk, P. Adamson, G. O. Hartley, C. W. Monroe, T. J. Marrow and P. G. Bruce, *Nat. Mater.*, 2021, **20**, 1121–1129.

43 S. Hao, S. R. Daemi, T. M. M. Heenan, W. Du, C. Tan, M. Storm, C. Rau, D. J. L. Brett and P. R. Shearing, *Nano Energy*, 2021, **82**, 105744.

44 Z. Ning, G. Li, D. L. R. Melvin, Y. Chen, J. Bu, D. Spencer-Jolly, J. Liu, B. Hu, X. Gao, J. Perera, C. Gong, S. D. Pu, S. Zhang, B. Liu, G. O. Hartley, A. J. Bodey, R. I. Todd,

P. S. Grant, D. E. J. Armstrong, T. J. Marrow, C. W. Monroe and P. G. Bruce, *Nature*, 2023, **618**, 287–293.

45 S. Yu and D. J. Siegel, *ACS Appl. Mater. Interfaces*, 2018, **10**, 38151–38158.

46 T. Fuchs, C. G. Haslam, A. C. Moy, C. Lerch, T. Krauskopf, J. Sakamoto, F. H. Richter and J. Janek, *Adv. Energy Mater.*, 2022, **12**, 2201125.

47 A. Müller, L. Paravicini, J. Morzy, M. Krause, J. Casella, N. Osenciat, M. H. Futscher and Y. E. Romanyuk, *ACS Appl. Mater. Interfaces*, 2024, **16**, 695–703.

48 S. H. Park, D. Jun, J. E. Jung, S. G. Lee, G. H. Lee and Y. J. Lee, *J. Mater. Chem. A*, 2022, **10**, 21995–22006.

49 P. Pietsch and V. Wood, *Annu. Rev. Mater. Res.*, 2017, **47**, 451–479.

50 S. Hao, J. J. Bailey, F. Iacoviello, J. Bu, P. S. Grant, D. J. L. Brett and P. R. Shearing, *Adv. Funct. Mater.*, 2021, **31**, 2007564.

51 B. Hu, S. Zhang, Z. Ning, D. Spencer-Jolly, D. L. R. Melvin, X. Gao, J. Perera, S. D. Pu, G. J. Rees, L. Wang, L. Yang, H. Gao, S. Marathe, G. Burca, T. J. Marrow and P. G. Bruce, *Joule*, 2024, **8**, 2623–2638.

52 S. E. Sandoval, F. J. Q. Cortes, E. J. Klein, J. A. Lewis, P. P. Shetty, D. Yeh and M. T. McDowell, *J. Electrochem. Soc.*, 2021, **168**, 100517.